Electronic Supplementary Information (ESI) for

Negative thermal quenching of photoluminescence in a copper–organic framework emitter

Ting Wu, Shenlong Jiang, Pabitra Narayan Samanta, Yangbin Xie, Jipeng Li, Xiaoling Wang, Devashis Majumdar, Xiangwei Gu, Yusong Wang, Wei Huang, Qun Zhang, Jerzy Leszczynski and Dayu Wu

Email: qunzh@ustc.edu.cn (Q. Z.); jerzy@icnanotox.org (J. L.); wudy@cczu.edu.cn (D. W.).

Experimental detail

Materials and characterizations. All the general reagents and solvents employed were commercially available and are used as received without further purification. CuI (99.9%) was purchased from Aldrich and used as received. The IR spectra were recorded on a Nicolet iS50 Fourier transform infrared spectrometer in the 4000−400 cm^{-1} range using KBr pellets. Elemental analyses (C, H, N) were performed using a PerkinElmer EA2400II elemental analyzer. Powder X-ray diffraction (PXRD) patterns were recorded on a Rigaku D/max 2500 PC with Cu Kα X-ray source (operated at 40 kV and 100 mA). Simulated PXRD patterns were calculated with CrystalDiffract (Copyright © 2015 CrystalMaker Software Ltd.) using the single-crystal cif file. Solid-state UV–vis spectra were recorded on a SHIMADZU UV-3600 UV−vis−NIR spectrophotometer. Fluorescence spectra were recorded at RT on an Edinburgh Model FS5 instrument. Emission and excitation spectra were also corrected for the spectral response of the monochromators and the detector, using typical correction spectra provided by the manufacturer. The measurements at low temperatures were performed using a liquid N_2 closed-cycle cryostat. The absolute emission quantum yields were measured using a quantum yield measurement system from Edinburgh with a 150 W xenon lamp coupled to a monochromator for wavelength discrimination, an integrating sphere as the sample chamber, and a multichannel analyzer for signal detection. PL decays were recorded using an Edinburgh FLS980 steady state fluorimeter with a time-correlated single-photon counting (TCSPC) spectrometer and a pulsed xenon lamp as the excitation source.

All the PL decay curves can be fitted to a single exponential function through the following equation

$$I(t) = A\ \exp(-t/\tau) \tag{1}$$

where I is the PL intensity, A is the pre-exponential coefficient, t is the time, and τ is the decay time. The results are displayed in Fig. 2d. Given a rapid thermal equilibrium between the two inter-convertible excited states (*i.e.*, S_1 and T_1), according to the TADF model the relationship between the decay time and temperature can be expressed by the following Boltzmann equation[1],

$$\tau(T) = \frac{3+exp\left[\frac{-\Delta E_{ST}}{k_B T}\right]}{\frac{3}{\tau(T_1)}+\frac{1}{\tau(S_1)}exp\left[\frac{-\Delta E_{ST}}{k_B T}\right]} \tag{2}$$

where $\tau(S_1)$ and $\tau(T_1)$ are the intrinsic decay times of the S_1 and T_1 states, respectively, ΔE_{ST} is the energy gap between the S_1 and T_1 states, and k_B is the Boltzmann constant.

Synthesis of 1,4-bis(imidazol-1-yl)but-2-ene (bibe). To a solution of imidazole (1.57 g, 13.3 mmol) in THF (50 mL) was added KOH (1.1 g, 20 mmol), the mixture was stirred at 50°C for 4 hours, then *trans*-1,4-dibromo-2-butene (0.7058g, 3.3 mmol) in THF (50 mL) was added dropwise. The reaction mixture was heated at 50°C overnight, which was then treated with deionized water (100 mL) after cooling at RT. The solution was extracted with methylene chloride three times, and the combined organic phases were concentrated in vacuum to give the white solid. Pure product was obtained after recrystallization with THF. ^{1}H NMR (400 MHz, $CDCl_3$): δ 7.46 (d, 1H), 7.17–7.03 (m, 1H), 6.89 (d, 1H), 5.75–5.72 (m, 1H), 4.60 (d, 2H). ^{13}C NMR (400 MHz, $CDCl_3$): 137.04, 129.85, 128.82, 118.94, 47.85. IR (KBr, ν, cm^{-1}): 1682(s), 1507(s), 1441(m), 1390(m), 1326(w), 1289(w), 1260(s), 1228(m), 1092(s), 968(s), 946(w), 919(m), 803(s), 736(s), 664(m), 626(s), 462(m).

Synthesis of bibeCu_4I_4. A mixture containing CuI (28.5mg, 0.15 mmol) and **bibe** (18.8 mg, 0.1 mmol) in 9 mL of H_2O/ CH_3CN (v/v, 2:1) was placed in a Parr Teflon-lined stainless steel vessel (20 mL) and then heated at 150 °C for 3 days under autogenous pressure. A large amount of brown needle crystals suitable for X-ray diffraction analysis was obtained after cooling the vessel to room temperature. The crystals were isolated, washed with H_2O/CH_3CN solvent, and dried under vacuum to give the final product. (yield: 56%). The purity of crystalline sample in batch is verified through the powder X-ray diffraction pattern and elemental micro-analysis (ESI Fig. 1). Anal. Calcd for $C_5H_6Cu_2I_2N_2$: C 12.64, H 1.27, N 5.90. Found: C, 12.71, H, 1.25, N, 5.93. IR (KBr, ν, cm^{-1}): 1598(w), 1516(s), 1435(m), 1398(w), 1365(m), 1273(m), 1234(s), 1106(s), 1085(m), 1065(w), 1024(m), 984(m), 937(m), 830(s), 744(s), 647(s), 622(m), 462(w).

X-ray crystal structure analysis. The diffraction intensity data were collected at 80, 100, 140, 180, 220, 260, and 298 K on a Bruker APEX-II CCD with graphite-monochromated Mo Kα radiation (λ = 0.71073 Å). Temperatures were controlled through slowly cooling a crystal over a period of 2 hours and annealing for 20 minutes at each temperature before data collection. Data collection, data reduction, and cell refinement were performed by using the Bruker Instrument Service v4.2.2 and SAINT V8.34A software[2,3]. Structure was solved using direct methods and refinement was performed using SHELXL based on F^2 through full-

matrix least-squares routine[4]. Absorption corrections were applied using multiscan program SADABS[5]. Hydrogen atoms of organic ligands were generated geometrically by the riding mode, and all the non-hydrogen atoms were refined anisotropically through full-matrix least-squares technique on F^2 with the SHELXTL program package[6,7]. The identical parameterization model was used for each temperature. A summary of the crystallographic data and refinement parameters was given in Table S1. The X-ray crystallographic coordinates for structures reported in this paper have been deposited at the Cambridge Crystallographic Data Center (CCDC), under deposition number CCDC 1975148, 1975149 and 1975151–1975155. These data can be obtained free of charge from The Cambridge Crystallographic Data Center via www.ccdc.cam.ac.uk/data_request/cif.

Femtosecond transient absorption (fs-TA) spectroscopy. The femtosecond transient absorption (fs-TA) spectroscopic characterizations are performed on a Helios-EOS pump–probe system (Ultrafast Systems LLC) under temperature-controllable conditions. During the measurements, a nitrogen cryostat (Optistat DN2, Oxford Instruments) equipped with a controller (MercuryiTC, Oxford Instruments) is used to control the temperature. The solid sample is held in place by two pieces of ultraviolet fused silica (thickness 0.5 mm). The pump pulses (centre wavelength at 340 nm; pulse energy ~10 nJ at the sample cell) are delivered by an optical parametric amplifier (TOPAS-800-fs), which is excited by a Ti: sapphire regenerative amplifier (Coherent Legend Elite-1K-HE; centre wavelength 800 nm, pulse duration 35 fs, pulse energy 3 mJ) seeded with a mode-locked Ti: sapphire laser system (Micra 5) and pumped with a 1-kHz Nd: YLF laser (Evolution 30). The white-light continuum probe pulses (500–800 nm) are generated by focusing a tiny portion of the 800-nm beam onto a sapphire plate. The instrument response function is determined to be ~80 fs by a routine cross-correlation procedure. The temporal and spectral profiles (chirp-corrected) of the pump-induced absorbance changes of the samples are registered using an optical fiber-coupled multichannel spectrometer and further processed by a Surface Xplorer software.

Solid-state NMR. All solid-state NMR experiments are carried out at the field of 9.4 T on a Bruker AVANCE III 400WB spectrometer. The ^{13}C signals are acquired at the resonance frequency of 100.63 MHz using a 4 mm double-resonance probe. The magic angle spinning rate is set to 14 kHz. As for the $^{1}H \rightarrow ^{13}C$ CP/MAS NMR experiments, the contact time is 2.0 ms and the repetition time is 2.0 s. The ^{13}C chemical shifts are referenced to tetramethylsilane

(TMS) and glycine (a second reference to TMS). The temperature is controlled by a Bruker temperature controller with a deviation of ±1.0 K. Below RT, the temperature is changed in 3 K/min intervals and a 90 min period is sufficient to allow temperature stabilization before collecting the data.

Raman spectra. Raman spectra are recorded with WITec alpha300 RAS+ confocal Raman microscopy (WITec GmbH). The excitation laser is a diode-pumped solid-state laser (532 nm, Cobolt Laser). A diffraction-limit spot size of the 532 nm laser is about 300 nm (with a 100 × objective, NA = 0.90). The Raman scattered light is dispersed by a 600 mm focal length spectrometer with a 600 or 1800 grooves/mm grating (UHTS 300). A nitrogen microscopy cryostat (RC102-CFM, CRYO Industries of America, Inc.) equipped with a controller (Lakeshore Model 335, Lake Shore Cryotronics, Inc.) is used to control the temperature.

Computational detail

In order to simulate the electronic absorption spectrum of the cluster model of **bibeCu$_4$I$_4$** molecular crystal, the vertical excitation energies and oscillator strengths are computed for a maximum of 100 spin-allowed and -forbidden low-lying singlet and triplet excited states within the framework of linear response time-dependent density functional theory (LR-TD-DFT) using CAM-B3LYP exchange-correlation functional as implemented in Gaussian16 code[8]. We have employed 6-31G(d) basis sets for the lighter atoms namely C, H, and N, while LANL2DZ basis sets and effective core potentials are used for the heavier Cu and I atoms. For the estimation of radiative and nonradiative decay rates, the vertical emission energies and transition dipole moments are calculated for the lowest singlet S_1 and triplet (T_1) excited states. The spin-relaxed open-shell calculations are carried out to optimize the geometry of the T_1 state, whereas the structural relaxation of the S_1 state is achieved by deploying implemented TD-DFT gradients. All the stationary points on the potential energy surface are confirmed from the harmonic vibrational frequency analysis. In order to encounter the gas-to-crystal phase shifts of the frontier-orbital quasi-particle energies in the solid-state material[9], the optimally tuned CAM-B3LYP functional obtained by combining the polarizable continuum model PCM ($\varepsilon = 2.37$) has been employed to predict the photoluminescence properties. For further refinement in the computation of fluorescence and phosphorescence spectra in solution, the state-specific (SS) approach[10,11] has been

implemented to reckon the dynamical solvation effects on LR-TD-DFT geometry relaxations. The emission energy within the SS-scheme (ΔE_{emi}^{SS}) is calculated by

$$\Delta E_{emi}^{SS} = E_{EQ}^{ES}(Q_0^{ES}) - E_{NEQ}^{GS}(Q_0^{ES}) \quad (3)$$

where $E_{EQ}^{ES}(Q_0^{ES})$ corresponds to the energy of the excited state (ES) with equilibrium solvation at the optimized excited state geometry (Q_0^{ES}), and $E_{NEQ}^{GS}(Q_0^{ES})$ refers to the energy of the ground state (GS) with non-equilibrium solvation at (Q_0^{ES}).

Next, the radiative decay rates (k_r) including the electronic-vibrational coupling, the shift of nuclear Cartesian coordinates between the ground and excited states and the Duschinsky rotation are calculated within a multimode harmonic oscillator model[12]. The total radiative decay rate constant is obtained by the integration over the whole emission spectrum,

$$k_r = \int \sigma_{emi}(\omega)\, d\omega \quad (4)$$

The rate of one photon emission is calculated by

$$\sigma_{emi}(\omega) = \frac{4\omega^3}{3\hbar c^3} \sum_{w',w} p_{w'} \left|\mu_{w',w}\right|^2 \delta(E_{w'} - E_w + \hbar\omega) \quad (5)$$

where $\mu_{w',w} = \langle e'|\langle w'|\mu|w\rangle|e\rangle$ are the transition dipole moments, $|w'\rangle$ and $|w\rangle$ are the vibrational states of state $|e'\rangle$ and $|e\rangle$, respectively; $E_{w'}$ and E_w denote their energies, and $p_{w'}$ refers to the Boltzmann distribution function for the initial-state vibronic manifold at the finite temperature. The line intensities in such one-photon emission processes are calculated by employing the Franck-Condon-Herzberg-Teller approximation of the electronic transition dipole moment within the framework of path-integral approach. The dipole autocorrelation function is computed by accounting the time-dependent solvent reaction field. Furthermore, for a reliable estimation of spin–orbit coupling (SOC) and zero-field splitting (ZFS) mediating $T_1 \rightarrow S_1$ reverse intersystem crossing (RISC), the quasi-degenerate perturbation theory (QDPT)[13] has subsequently exploited to evaluate the mixing between singlet and triplet manifolds obtained from TD-DFT. The SOC calculations are carried out using ORCA 4.2 program at the TD-B3LYP/ DEF2-TZVP level with LR-CPCM energy corrections for the solvent[14]. Herein, we consider spin–orbit mean-field (SOMF) of the Breit-Pauli SOC operator on all atomic centers, where the spin-same orbit and spin-other orbit interactions as well as the exchange effects are accounted explicitly.

Finally, in the limit of Franck-Condon approximation, the rate constant of the nonradiative RISC process within the non-adiabatic regime is estimated by invoking the Fermi's Golden rule approximation and neglecting the spin-vibronic perturbation terms[15],

$$k_{RISC} = \frac{2\pi}{\hbar}\sum_{\gamma}\left|\langle S_i|\hat{H}_{SOC}|T_f^{\gamma}\rangle\right|_{q_0}^2 \rho_{FCWD} \quad (6)$$

where γ refers to the ZFS spin-sublevels; i and f designate the electronic states of the singlet and triplet multiplicity, respectively. ρ_{FCWD} describes the Franck-Condon-weighted density of states that relies on the evaluation of thermokinetic barrier associated with the RISC process. The ρ_{FCWD} is calculated by using the semiclassical Marcus theory,

$$\rho_{FCWD} = \frac{1}{\sqrt{4\pi\lambda k_B T}} exp\left[-\frac{(\Delta E_{ST} + \lambda)^2}{4\lambda k_B T}\right] \quad (7)$$

where ΔE_{ST} is the energy gap between the S_1 and T_1 states at their equilibrium geometries. The reorganization energy λ is defined as the energy required to bring the system in the S_1 to the minimum structure of the T_1 state. The values of λ are calculated by deploying two-point method based on the following excitation energies

$$\lambda = E_{S_1}(T_1) - E_{S_1}(S_1) \quad (8)$$

where $E_{S_1}(T_1/S_1)$ refers to the energy of the S_1 state at the T_1/S_1 equilibrium geometry.

Supplementary Figures

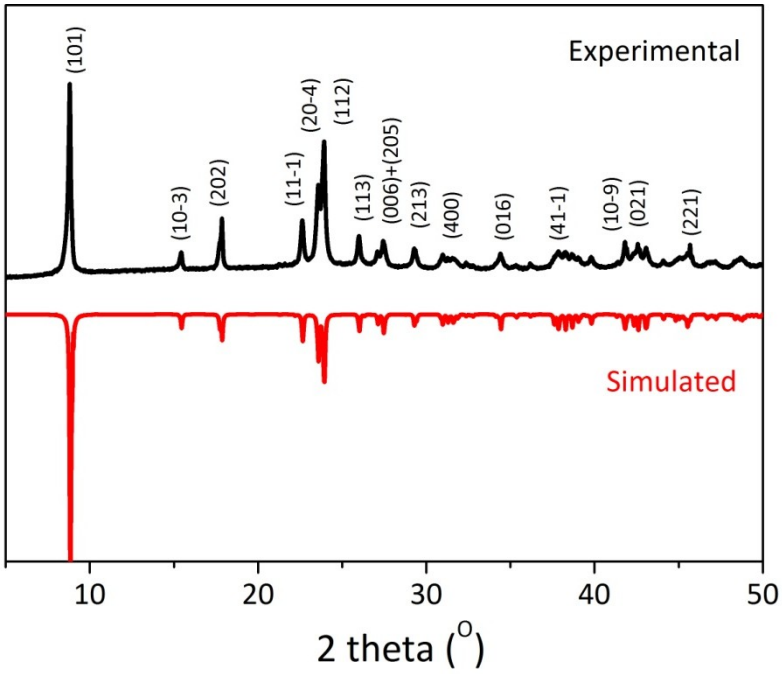

Fig. S1

The PXRD pattern of crystalline sample **bibeCu$_4$I$_4$** as well as the simulated pattern.

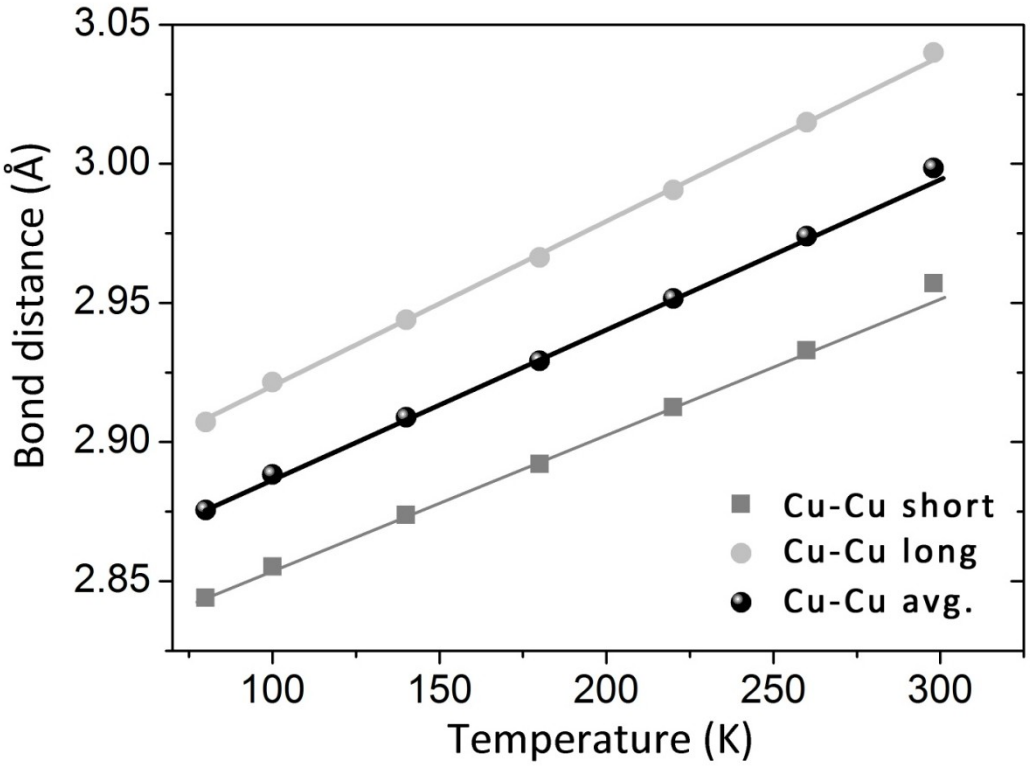

Fig. S2

Cu···Cu distances [Å] of **bibeCu$_4$I$_4$** at different temperatures.

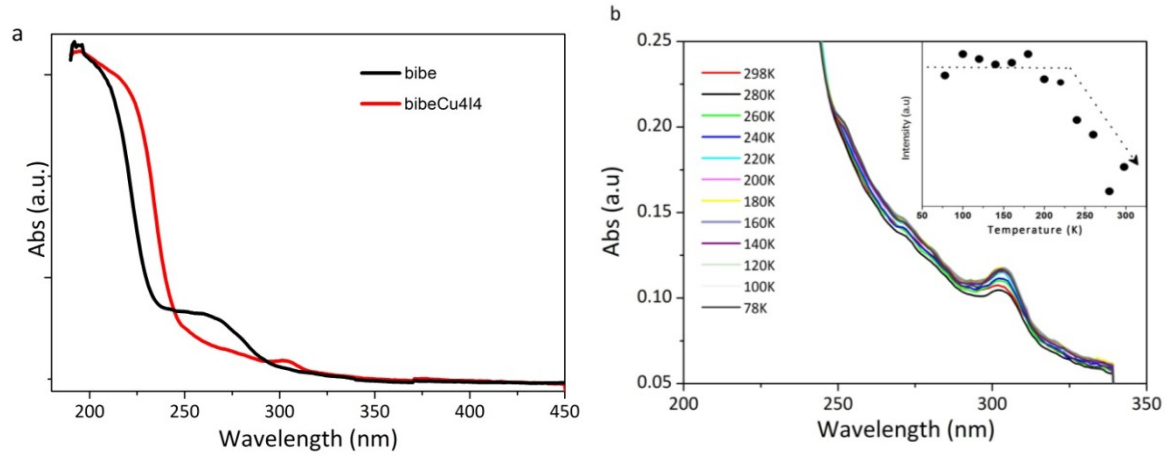

Fig. S3 The electronic absorption spectra. The experimental spectra (**a**) of **bibe** and **bibeCu$_4$I$_4$** crystals in thin films at RT (298 K). The electronic absorption spectra of **bibeCu$_4$I$_4$** crystal (**b**) in thin film at different temperatures.

The electronic absorption spectra below 240 K exhibit the relatively strong absorption peak in the UV region and almost keep unchanged with temperature, while the intensity continues to decrease with increasing temperatures from 240 K to RT, reflecting an electronic structural transition of **bibe** ligand.

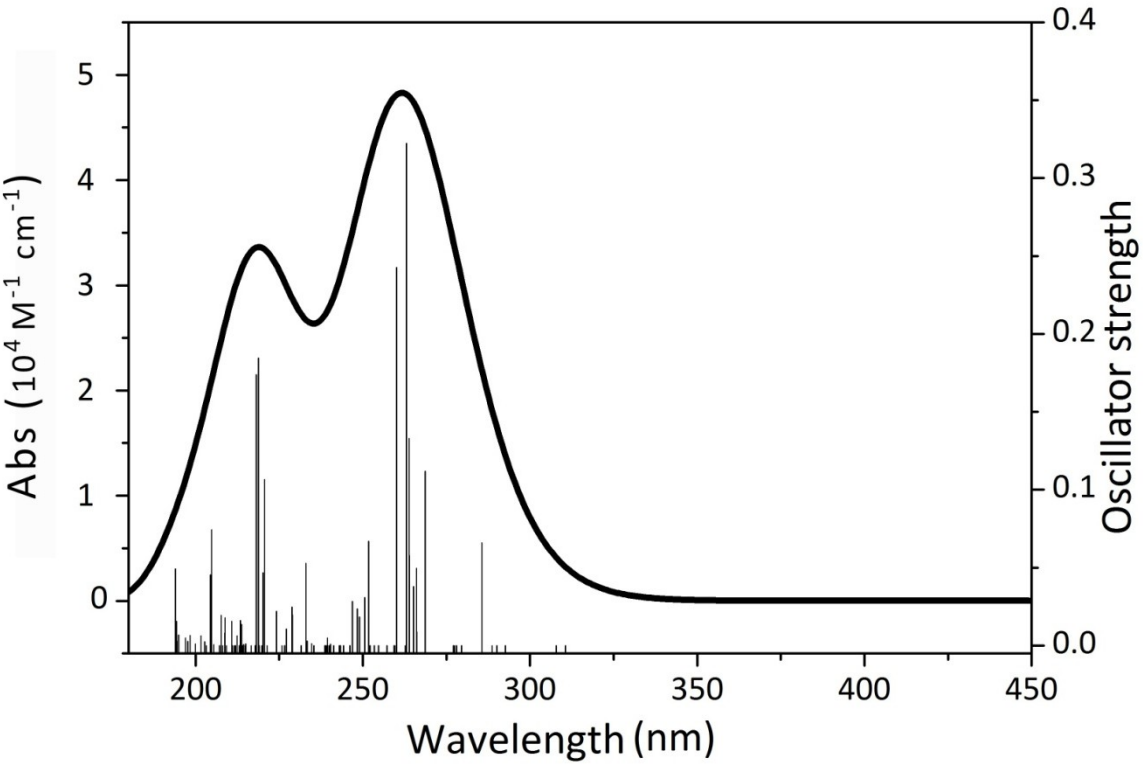

Fig. S4 Simulated electronic absorption spectra.

The absorption spectra of **bibeCu$_4$I$_4$** at 298 K is simulated through the LR-CPCM/TD-CAM-B3LYP level of theory. The estimated maximum absorption wavelength (λ_{max}) is appeared to be at 263 nm that agrees well with the experimental absorption spectra of **bibe** and **bibeCu$_4$I$_4$** crystals recorded at room temperature (298 K). Furthermore, the temperature dependence of the electronic absorption spectra (Supplementary Fig. 3b) reveals a weak band at ~300 nm, which is retained in the computed spectra at 286 nm. The calculated vertical excitation energies (E_{ex}), oscillator strengths (f), dipole strengths (S) and major contributions of the molecular orbitals (MOs) for the electronic excitations with $f > 0.05$ were provided in Supplementary Table 2.

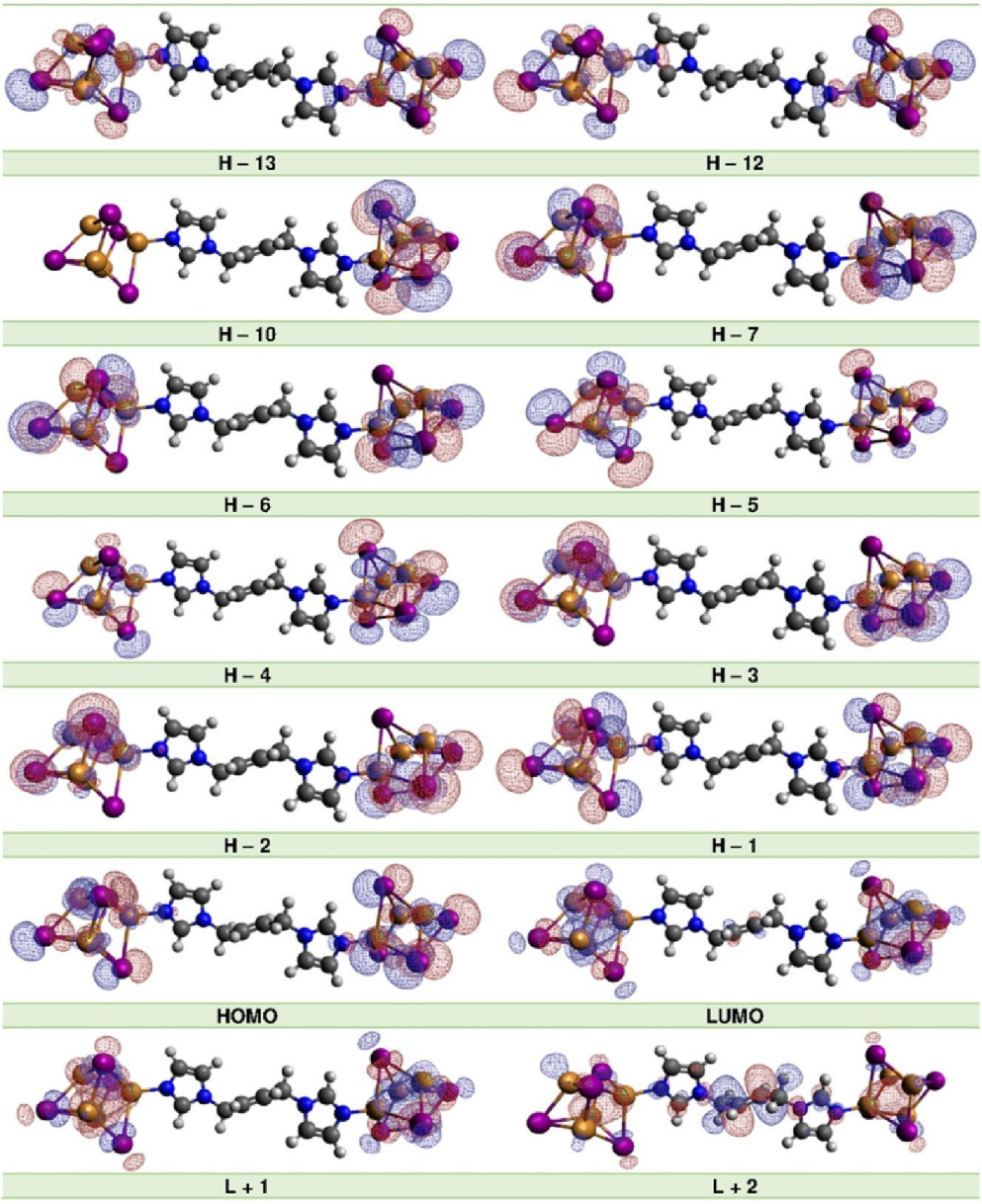

Fig. S5

Selected frontier molecular orbitals responsible for the low-lying electronic transitions corresponding to the electronic absorption spectrum of **bibeCu$_4$I$_4$**.

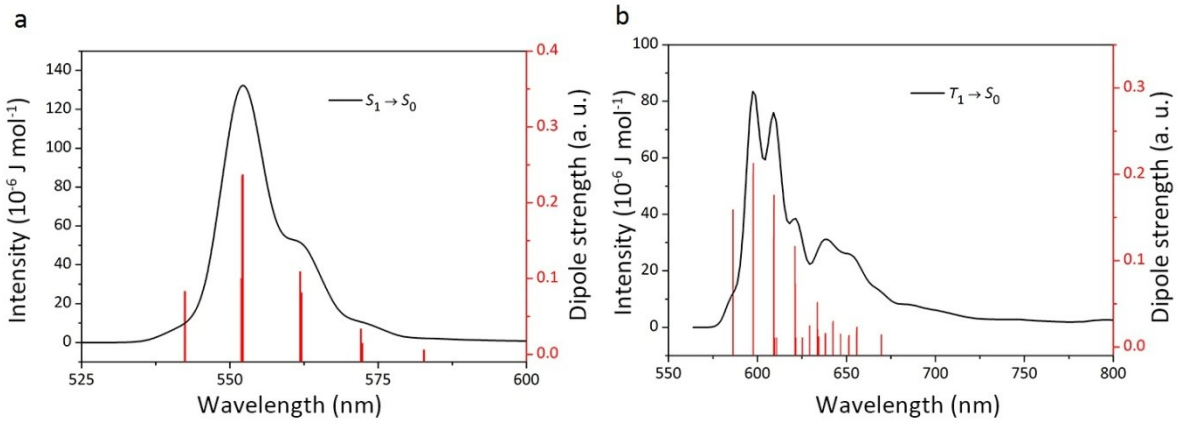

Fig. S6 DFT calculated PL emission spectra. Vibrationally resolved emission spectra in **a** and **b** correspond to fluorescence and phosphorescence transition.

The calculated $0-0$ transition energies (ΔE_{00}) by accounting the distortion effect of the potential energy surfaces, *i.e.* the Duschinsky rotation effect, are found to appear at 552 nm and 598 nm, respectively, for the radiative $S_1 \rightarrow S_0$ and $T_1 \rightarrow S_0$ transitions.

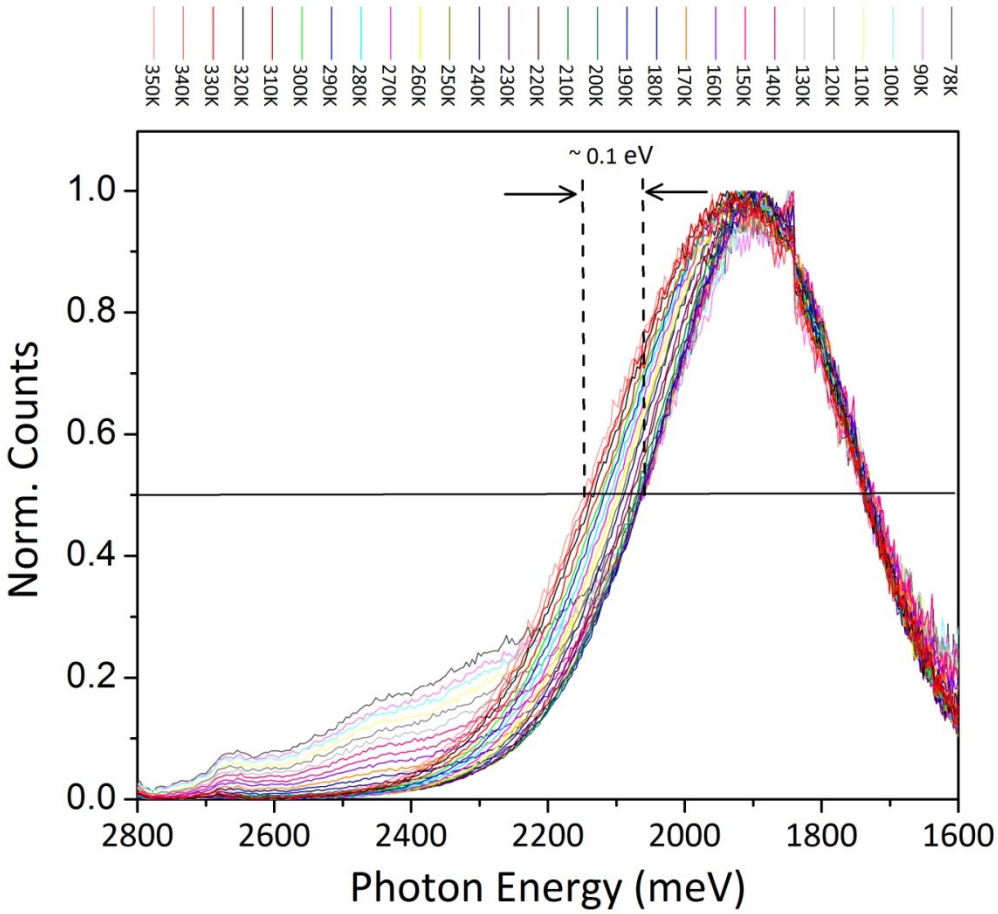

Fig. S7 The normalized emission spectra of bibeCu_4I_4 at different temperatures.

The blue shift of the emission spectra with increasing temperature is clearly visible at the blue edge.

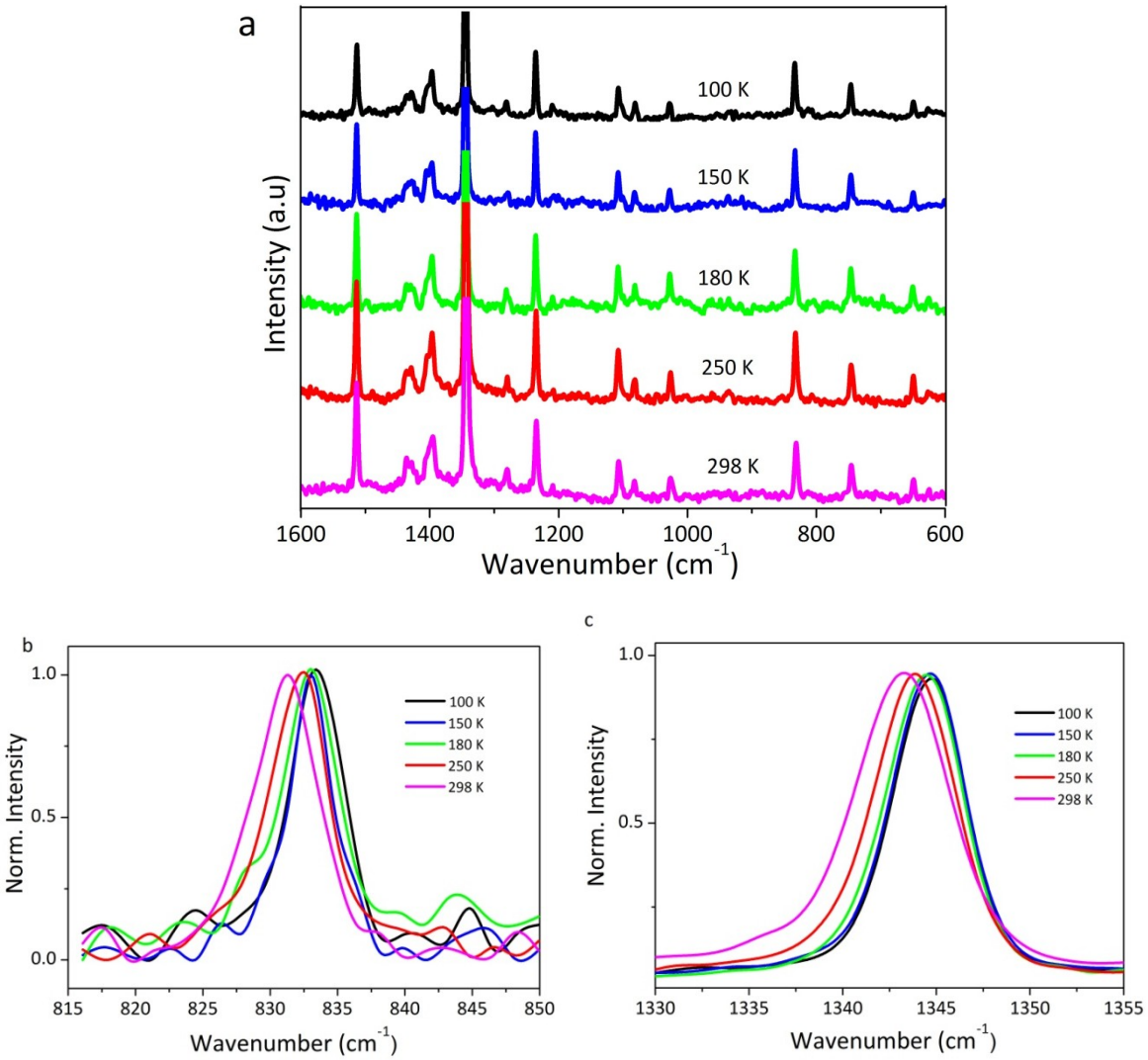

Fig. S8 The Raman spectra at different temperatures. Full spectra of **bibeCu$_4$I$_4$** (**a**) in the range of 600–1600 cm^{-1}. In **b** and **c**, the normalized spectra in the selected bands are shown for clarity.

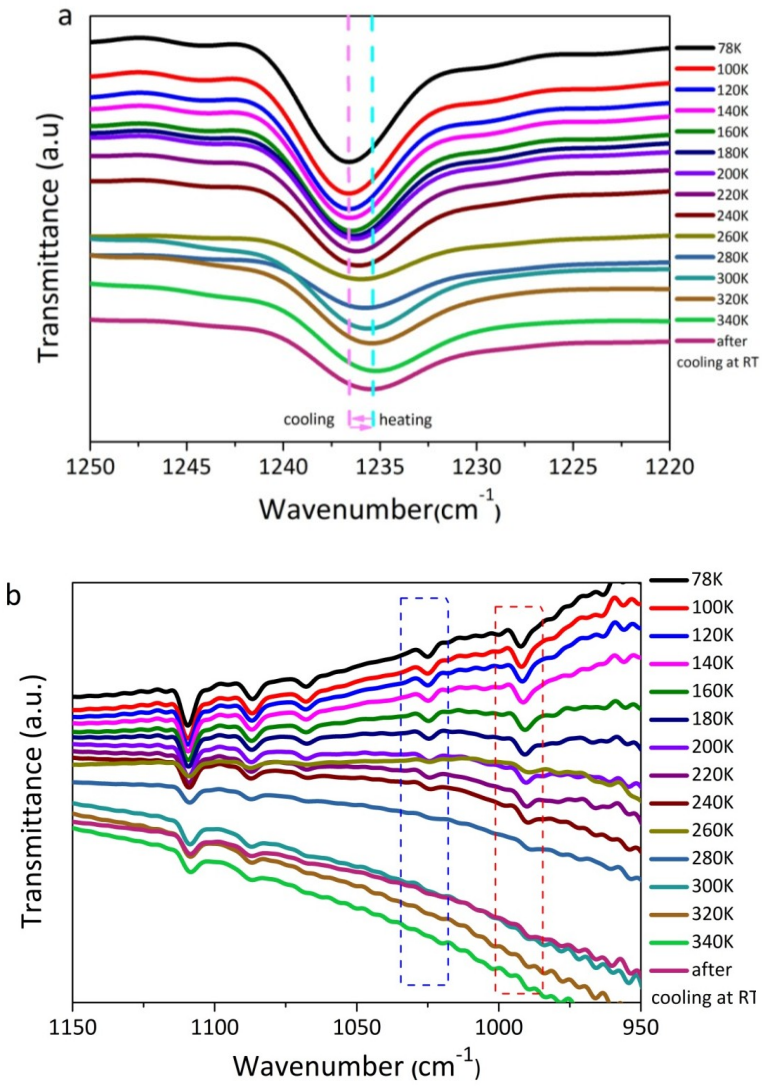

Fig. S9 The variable-temperature FT-IR spectra at the selected ranges.

Upon heating the sample in the atmosphere of liquid nitrogen, both peak shape and position at band of 1236 cm^{-1} in **a**, assignable to the imidazole skeleton, show abrupt change at 260 K. In **b**, the peaks at *ca.* 990 and 1068 cm^{-1}, corresponding to the small fraction of C–C and C–N single bonds in imidazole ring, continue to decrease above 260 K. The spectral response indicates that the population of resonance structure begins to decreases with increasing temperatures[16].

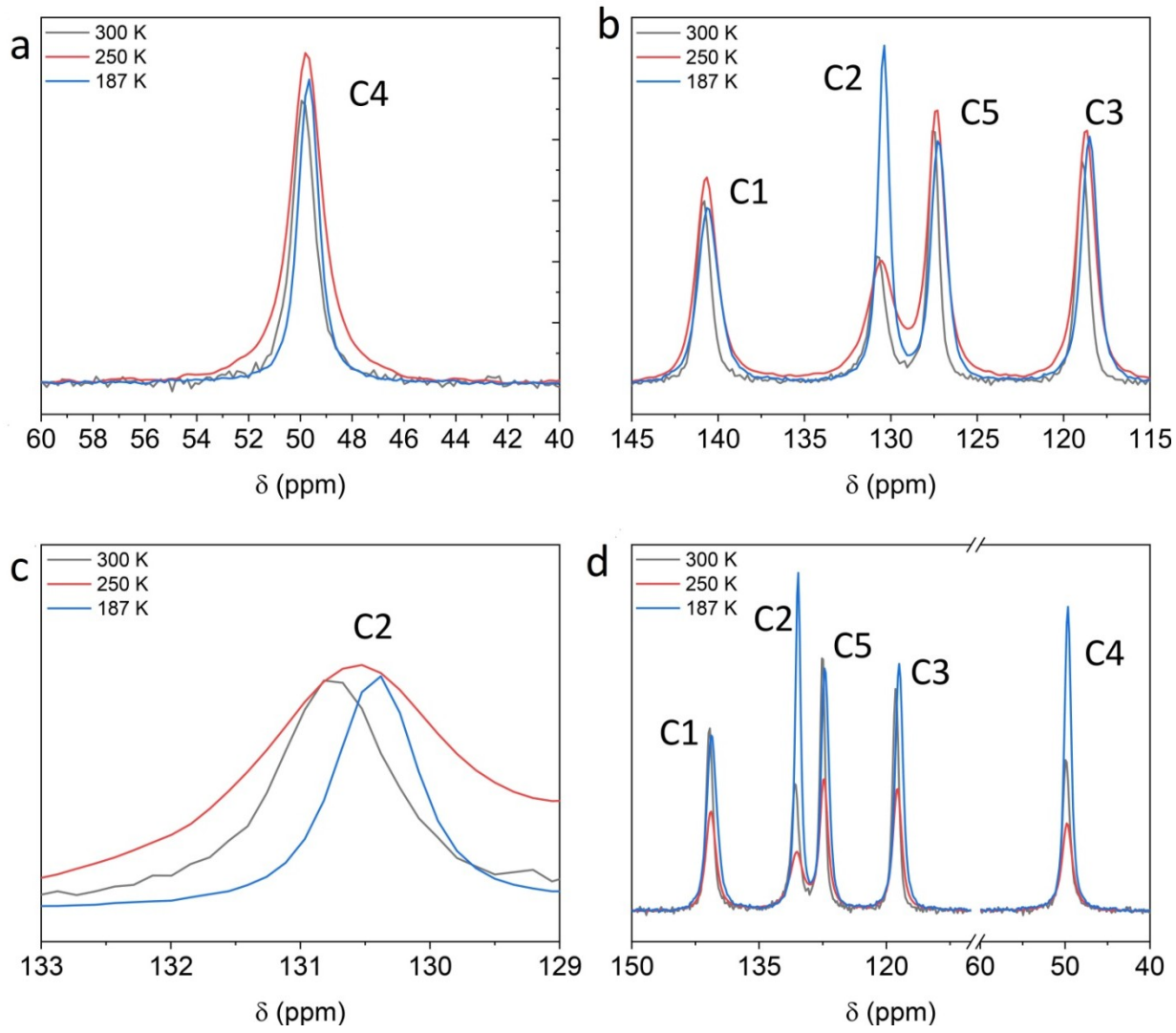

Fig. S10 Solid-state ^{13}C NMR spectrum. The normalized spectra of the C4 chemical-shift range of **bibeCu$_4$I$_4$** at the varied temperatures in **a**. The normalized spectra (**b**) of the C1, C5, and C3 chemical-shift range of **bibeCu$_4$I$_4$** at the varied temperatures. The normalized spectra (**c**) with partial magnification of the C2 chemical-shift range of **bibeCu$_4$I$_4$** at the varied temperatures. The actual spectra (**d**) of **bibeCu$_4$I$_4$** at the varied temperatures.

Supplementary Tables

Table S1. Crystal data collection and structure refinement for **bibeCu$_4$I$_4$**.

Temperature/K	80(2)	100(2)	140(2)	180(2)	220(2)	260(2)	298(2)
Formula	$C_5H_6Cu_2I_2N_2$	$C_5H_6Cu_2I_2N_2$	$C_5H_6Cu_2I_2N_2$	$C_5H_6Cu_2I_2N_2$	$C_5H_6Cu_2I_2N_2$	$C_5H_6Cu_2I_2N_2$	$C_5H_6Cu_2I_2N_2$
Formula weight	475.00	475.00	475.00	475.00	475.00	475.00	475.00
Crystal system	monoclinic	monoclinic	monoclinic	monoclinic	monoclinic	monoclinic	monoclinic
Space group	$P2_1/n$	$P2_1/n$	$P2_1/n$	$P2_1/n$	$P2_1/n$	$P2_1/n$	$P2_1/n$
a [Å]	11.4617(4)	11.4724(4)	11.4918(4)	11.5103(4)	11.5218(14)	11.5363(6)	11.5380(6)
b [Å]	4.22060(10)	4.22380(10)	4.23200(10)	4.24120(10)	4.2497(2)	4.2584(2)	4.2653(2)
c [Å]	19.5436(6)	19.5467(6)	19.5567(7)	19.5894(9)	19.6222(8)	19.6624(12)	19.7023(13)
β [º]	90.441(3)	90.445(3)	90.451(3)	90.446(3)	90.458(4)	90.490(5)	90.478(5)
V [Å^3]	945.40(5)	947.15(5)	951.08(5)	956.28(5)	960.75(7)	965.90(9)	969.58(9)
Z	4	4	4	4	4	4	4
ρ_{calcd} [g cm^{-3}]	3.337	3.331	3.317	3.299	3.284	3.266	3.254
R_{int}	0.0378	0.0625	0.0456	0.0511	0.0896	0.0974	0.1390
μ (Mo-K$_\alpha$) [mm^{-1}]	10.967	10.947	10.902	10.842	10.792	10.734	10.694
***F* (000)**	856	856	856	856	856	856	856
GOF[a] on F^2	1.049	1.043	1.080	1.060	1.051	1.014	1.578
R_1[b]/wR_2[c][I>2σ(I)]	0.0286/0.0737	0.0411/0.1092	0.0363/0.0911	0.0381/0.1035	0.0590/0.1513	0.0828/0.2266	0.1505/0.3532
R_1/wR_2(all date)	0.0311/0.0750	0.0436/0.1115	0.0389/0.0927	0.0417/0.1061	0.0647/0.1567	0.0968/0.2506	0.1673/0.3900

[a] Goodness-of-fit = $[[w(F_0^2-F_c^2)^2]/(N_{obs}-N_{params})]^{1/2}$, based on the data $I>2\sigma(I)$.

[b] $R_1 = \sum||F_0|-|F_c||/\sum|F_0|$. [c] $wR_2 = \{\sum[w(F_o^2-F_c^2)^2]/\sum[w(F_0^2)^2]\}^{1/2}$

Table S2. Calculated excitation energies (E_{ex}), oscillator strength (f), dipole strength (S) and major contribution of molecular orbitals for the low-lying excited states of the ground state equilibrium geometry of **bibeCu$_4$I$_4$** at the PCM-tuned TD-CAM-B3LYP/6-31G(d)//LANL2DZ level of theory.

State	E_{ex} (nm)	f	S(a.u)	Assignment (%)
S_0	286	0.066	0.62	H-1 → L+1 (29), H → L (29)
	269	0.112	0.99	H-7 → L+1 (18), H-6→ L (11), H-3 → L+1 (13), H-2 → L (12)
	264	0.133	1.15	H-10 → L (14), H-10 → L+1 (17)
	263	0.322	2.79	H-5 → L (15), H-5 → L+1 (13), H-4 → L (11), H-4 → L+1 (11)
	260	0.243	2.08	H-13 → L+1 (23), H-12 → L (23)

Table S3. Computed spin–orbit coupling matrix elements (SOCME) followed by average spin–orbit coupling constant (SOCC) between the triplet ($\boldsymbol{T_m}$) and singlet ($\boldsymbol{S_n}$) manifolds using the RI-SOMF(1X) approximation within the framework of combined QDPT/TD-DFT approaches. [All the values are in cm^{-1}.]

Root		$\langle \boldsymbol{T_m} \vert \widehat{\boldsymbol{H}}_{\boldsymbol{SOC}} \vert \boldsymbol{S_n} \rangle$			$\boldsymbol{SOCC}^{a}$
$\boldsymbol{T_m}$	$\boldsymbol{S_n}$	**Z**	**X**	**Y**	
$\boldsymbol{T_1}$	S_1	61.62	–5.83	3.92	20.67
	S_2	150.09	–8.36	3.96	50.12
	S_3	–2.03	–93.40	51.05	35.49
	S_4	–0.45	24.92	94.41	32.55
	S_5	–0.11	0.03	–0.66	0.22
	S_6	0.21	30.91	41.01	17.12
	S_7	–73.88	8.10	–9.37	24.97
	S_8	–0.21	–0.76	3.34	1.14
	S_9	–0.11	–0.23	0.93	0.32
	S_{10}	0.43	–3.84	14.95	5.15

[a] $SOCC = \frac{1}{3}\sqrt{\left|\langle T_m|\widehat{H}_{SOC}|S_n\rangle_X\right|^2 + \left|\langle T_m|\widehat{H}_{SOC}|S_n\rangle_Y\right|^2 + \left|\langle T_m|\widehat{H}_{SOC}|S_n\rangle_Z\right|^2}$

Supplementary References

1. M. J. Leitl, D. M. Zink, A. Schinabeck, T. Baumann, D. Volz and H. Yersin, *Top Curr. Chem.* 2016, **374**, 25.
2. SAINT, v8.34A. Bruker AXS. Madison, Wisconsin, USA, 2013.
3. APEX2, v2014.1. Bruker AXS. Madison, Wisconsin, USA, 2009.
4. G. M. Sheldrick, *Acta Crystallogr.* 2008, **A64**, 112−122.
5. SADABS. Bruker AXS. Madison, Wisconsin, USA, 2014.
6. Bruker Advanced X-ray Solutions, SHELXTL, v6. 14. Bruker AXS Inc. Madison, Wisconsin, USA, 2003.
7. A. L. Spek. *J. Appl. Cryst.* 2003, **36**, 7−13.
8. M. J. Frisch, G. W. Trucks, H. B. Schlegel, G. E. Scuseria, M. A. Robb, J. R. Cheeseman, G. Scalmani, V. Barone, B. Mennucci, G. A. Petersson, H. Nakatsuji, M.Caricato, X. Li, H. P. Hratchian, A. F. Izmaylov, J. Bloino, G. Zheng, J. L. Sonnenberg, M. Hada, M. Ehara, K. Toyota, R. Fukuda, J. Hasegawa, M. Ishida, T. Nakajima, Y. Honda, O. Kitao, H. Nakai, T. Vreven, J. A. Montgomery, Jr., J. E. Peralta, F. Ogliaro, M. Bearpark, J. J. Heyd, E. Brothers, K. N. Kudin, V. N. Staroverov, R. Kobayashi, J. Normand, K. Raghavachari, A. Rendell, J. C. Burant, S. S.Iyengar, J. Tomasi, M. Cossi, N. Rega, N. J. Millam, M. Klene, J. E. Knox, J. B. Cross, V. Bakken, C. Adamo, J. Jaramillo, R. Gomperts, R. E. Stratmann, O. Yazyev, A. J. Austin, R. Cammi, C. Pomelli, J. W. Ochterski, R. L. Martin, K.Morokuma, V. G. Zakrzewski, G. A. Voth, P. Salvador, J. J. Dannenberg, S. Dapprich, A. D. Daniels, Ö. Farkas, J. B. Foresman, J. V. Ortiz, J. Cioslowski and D. J. Fox, Gaussian 16, revision C.01; Gaussian, Inc.: Wallingford CT, 2016.
9. H. Sun, S. Ryno, C. Zhong, M. K. Ravva, Z. Sun, T. Körzdörfer and J.-L. Brédas, *J. Chem. Theory Comput.* 2016, **12**, 2906−2916.
10. R. Improta, V. Barone, G. Scalmani and M. J. Frisch, *J. Chem. Phys.* 2006, **125**, 054103.
11. R. Improta, G. Scalmani, M. J. Frisch and V. Barone, *J. Chem. Phys.* 2007, **127**, 074504.

12. F. Santoro, R. Improta, A. Lami, J. Bloino and V. Barone, *J. Chem. Phys.* 2007, **126**, 084509-1-13.
13. B. de Souza, G. Farias, F. Neese and R. Izsák, *J. Chem. Theory Comput.* 2019, **15**, 1896–1904.
14. F. Neese, The ORCA program system. *WIREs Comput. Mol. Sci.* 2012, **2**, 73–78.
15. J. L. Brédas, D. Beljonne, V. Coropceanu and J. Cornil, *Chem. Rev.* 2004, **104**, 4971–5003.
16. I. Sidir, Y. G. Sidir and I. Kayagil, *Spectrochimica Acta Part A–Molecular and Biomolecular Spectroscopy*. 2011, **81**, 339–352.